INTERNATIONAL JOURNAL FOR NUMERICAL METHODS IN FLUIDS
Int. J. Numer. Meth. Fluids 2006; **51**:773–790
Published online 28 December 2005 in Wiley InterScience (www.interscience.wiley.com). DOI: 10.1002/fld.1158

Wave kinematic fields from the boundary integral method

Rodney J. Sobey*,†

Department of Civil and Environmental Engineering, Imperial College London, London SW7 2AZ, U.K.

SUMMARY

The predictive potential of interior domain solutions from the boundary integral method for 2D extreme wave kinematics is explored. Comparisons with analytical solutions for near-limit waves confirms the susceptibility of the boundary integral method to poor precision at near-boundary locations. Additionally, these comparisons identify a domain-wide precision challenge that is associated with the relatively rapid changes in water surface geometry and kinematics that are typical of extreme waves. A numerical evaluation of Green's integral around the boundary addresses these precision issues through formulation of the integration as a simultaneous system of ordinary differential equations at a cubic level of approximation. Careful attention is given to consistent interpolation of all contributions to the Green's integral. Copyright © 2005 John Wiley & Sons, Ltd.

KEY WORDS: boundary integral method; extreme waves; numerical code; potential flow; unsteady flow; wave kinematics

1. INTRODUCTION

Highly accurate solutions for the kinematics in extreme but regular waves in two space dimensions have been routine for several decades through analytical Stokes and cnoidal wave theories and the hybrid analytical-numerical Fourier approximation wave theory. But equivalent precision in the prediction of the kinematics in extreme but irregular waves has been a somewhat illusive objective.

The boundary integral method has long promised resolution of these difficulties. Existing codes have promised much, but have yet to demonstrate that they extend to the more extreme wave events.

The ultimate objective here is the investigation of the kinematics in 2D extreme waves. Nonlinear wave theory is being pushed to its limits. The mathematical physics must not be compromised at any step of the numerical solution. Numerical precision is imperative.

*Correspondence to: Rodney J. Sobey, Department of Civil and Environmental Engineering, Imperial College London, London SW7 2AZ, U.K.
†E-mail: r.j.sobey@imperial.ac.uk

Contract/grant sponsor: UK EPSRC; contract/grant number: GR/R64971/01(P)

Received 25 August 2005
Revised 8 November 2005
Accepted 12 November 2005

There are two separate and sequential problems in application of the boundary integral method to the prediction of wave kinematics:

(I) Solution for the unsteady evolution of the boundary kinematics, the boundary location (x,z), the velocity potential function ϕ and the outward normal gradient $\partial\phi/\partial n$ of the velocity potential function, at the boundary of the solution domain.
(II) Solution for the complete kinematics, in this case just the velocity potential function ϕ, throughout the interior of the solution domain.

The interior problem II is the easier problem, but the interdependence is important. The boundary problem I requires solution for ϕ around the boundary of the solution domain. The interior problem II requires solution for ϕ throughout the interior of the solution domain, which includes locations immediately adjacent to the boundary. For consistent precision, parallel algorithms are adopted for both problems. If this algorithm is in any way unsatisfactory for the interior problem, the difficulties will be compounded in the boundary problem, where evolution of the water surface is driven by the nonlinear boundary kinematics.

Attention is specifically directed to locations immediately adjacent to the boundaries, for a number of reasons:

1. The wave kinematics (velocities, accelerations, etc.) are most extreme at and near to the water surface.
2. The unique nature of a particular solution field is mostly driven by the lateral boundaries, which provide the essential boundary forcing (incident wave conditions, wave maker, coastal structure, sea wall, shoaling beach, etc.).
3. Nodal interpolation and hence numerical precision is often weakest at and near the boundaries.

Attention is directed to the interior problem II, the prediction of the interior kinematics in a wave tank (x,z) geometry. The ultimate need to accommodate a wave basin (x,y,z) geometry is acknowledged, but many of the crucial issues must first be resolved and proven for the geometrically simpler wave tank. Subsequent extension to a wave basin would involve a more complicated geometry and very significantly additional computational resources, but no new fluid mechanic challenges.

Literature attention to the interior problem II is sparse. There has been steady progress for the related boundary problem II, initiated by Longuet-Higgins and Cokelet [1] with further contributions, among others, from References [2–5]. Reference [6] is a useful review paper on the numerical wave tank problem, the boundary problem II. To date, Reference [7] is perhaps the most comprehensive extension to 3 spatial dimensions, though again attention does not extend to the interior problem.

2. BOUNDARY INTEGRAL METHOD

The basis of the boundary integral method is a closed (x,z) domain (Figure 1) in which the kinematics follow the Laplace equation

$$\frac{\partial^2\phi}{\partial x^2}+\frac{\partial^2\phi}{\partial z^2}=0 \tag{1}$$

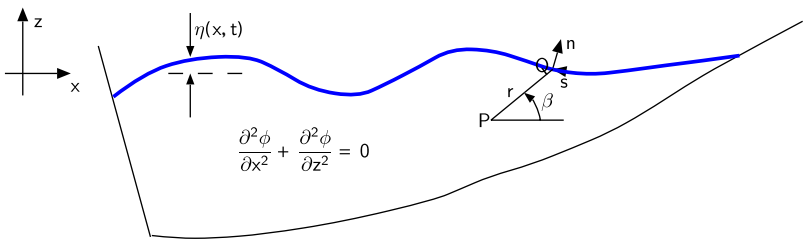

Figure 1. Solution domain.

where $\phi(x,z,t)$ is the velocity potential function in spatial coordinates x horizontal and z vertical and t is time. If the function $G(x,z,t)$ also satisfies the Laplace Equation (1) over the same domain, then Green's theorem [8] requires that

$$\int_S \left(\phi \frac{\partial G}{\partial n} - G\frac{\partial \phi}{\partial n}\right) \mathrm{d}s = 0 \tag{2}$$

over the boundary S of the closed domain. The boundary S is described by orthogonal curvilinear (s,n) coordinates (see Figure 1); s is directed anti-clockwise around the closed boundary so that n is the outwardly-directed normal.

If $G = \ln r$, where r is measured from any point P within S to the domain boundary at Q, then

$$-\alpha_P \phi_P = \int_S \left(\phi \frac{1}{r}\frac{\partial r}{\partial n} - \ln r \frac{\partial \phi}{\partial n}\right) \mathrm{d}s = G_B + G_C \tag{3}$$

where α_p is the angle surrounding P and wholly within the domain S. For an interior point, $\alpha_P = 2\pi$. For the boundary problem I, P is located on the boundary and $\alpha_P \neq 2\pi$.

Time t does not appear explicitly in Equation (3), but steady flow is not assumed. Equation (3) defines the instantaneous kinematics. The time-dependence and the non-linearity enter through the boundary conditions, which define the instantaneous (x,z) location of the boundary and the instantaneous value of either ϕ or $\partial\phi/\partial n$ at the boundary.

Numerical implementation of the boundary integral method is based, in principle, on Equation (3), with P located at discrete nodal points on the boundary S for problem I and inside the boundary for problem II. For problem II, the boundary variables, ϕ and $\partial\phi/\partial n$ at the boundary nodes, are known for each boundary location, and the problem is linear.

A major difficulty is identified in Equation (3) for near boundary nodes where r becomes very small. There are singularities where $r = 0$; $1/r \to \infty$ in the first part (G_B) of the integrand and $-\ln(r) \to \infty$ in the second part (G_C). r is never zero for problem II but it can be very near zero. For r near zero, both of these contributions become very large. As $1/r$ approaches ∞ much more rapidly than $-\ln(r)$, it is advantageous to adopt the identity $(1/r)(\partial r/\partial n) = \mathrm{d}\beta/\mathrm{d}s$ in the G_B part, following Reference [1]. The G_B term can be rewritten as

$$G_B = \int_S \phi \frac{1}{r}\frac{\partial r}{\partial n}\,\mathrm{d}s = \int_S \phi \frac{\mathrm{d}\beta}{\mathrm{d}s}\,\mathrm{d}s \tag{4}$$

Conveniently, the $\mathrm{d}\beta/\mathrm{d}s$ contribution remains finite and continuous.

For the G_C integral in the interior of the domain, $-\ln(r)$ becomes large quite slowly and r does not reach zero. The G_C or $\partial\phi/\partial n$ part of Green's integral is smooth and continuous over a boundary segment.

Summarizing, the Green's integral in the interior may be written as

$$-2\pi\phi_P = G_B + G_C = \int_S \phi \frac{\mathrm{d}\beta}{\mathrm{d}s}\,\mathrm{d}s - \int_S \ln r \frac{\partial\phi}{\partial n}\,\mathrm{d}s \tag{5}$$

Equation (5) remains exact. The specific context, kinematics in extreme waves, pushes nonlinear wave theory to its limits. Fidelity in the numerical implementation is important, in not succumbing to compromise in the choice of algorithms and in the code implementation.

3. NUMERICAL EVALUATION OF GREEN'S INTEGRAL

The boundary of the solution domain (see Figure 2) is identified as segments between geometric discontinuities at corners, there being $k_S = 1 \ldots K$ such segments. Each segment extends over nodes $j = j_F(k_S) \ldots j_L(k_S)$, from the first node j_F to the last node j_L.

Integration on the right-hand side of Equation (5) becomes the summation over consecutive inter-nodal intervals

$$-2\pi\phi_P = \sum_{k_S=1}^{K} \sum_{j=j_F(k_S)}^{j_L(k_S)-1} (\Delta G_B|_{i_P,j} + \Delta G_C|_{i_P,j}) \tag{6}$$

where the inter-nodal integrands are

$$\Delta G_B|_{i_P,j} = \int_{s_j}^{s_{j+1}} \phi \frac{\mathrm{d}\beta}{\mathrm{d}s}\,\mathrm{d}s, \quad \Delta G_C|_{i_P,j} = -\int_{s_j}^{s_{j+1}} \ln(r) \frac{\partial\phi}{\partial n}\,\mathrm{d}s \tag{7}$$

where i_P is the unique internal node location of P. Equation (6) is still exact.

Specific evaluation of the definite integrals in Equation (7) requires local interpolation between nodes. All numerical methods (finite difference, finite element, etc.) must adopt some manner of local interpolation. The potential for compromise is introduced in the numerical evaluation of the inter-nodal integrations in Equation (7), through the nature of the local interpolation and through the manner of integration.

In most cases the effective interpolation is polynomial, locally linear, quadratic, ... corresponding to first, second, ... order local approximations. The following discussion adopts locally cubic interpolation, the dependent variable $f(=\phi$ or $\partial\phi/\partial n)$ being:

$$f(s) = f_0 + f_1 s + f_2 s^2 + f_3 s^3 \tag{8}$$

where s is the dependent variable around the boundary of the domain (Figure 1). The locally-constant coefficients $f_0 \ldots f_3$ are evaluated uniquely from the consecutive nodal locations s_{j-1}, s_j, s_{j+1}, s_{j+2} and the local $f(s)$ values at these consecutive nodes. Inter-nodal integration is over the two central nodes, from s_j to s_{j+1}.

Evaluation of the Green's integral, Equation (7), requires the curvilinear boundary coordinate s_j and the angle β_j at each of the boundary nodes. Each node is specified by its Cartesian

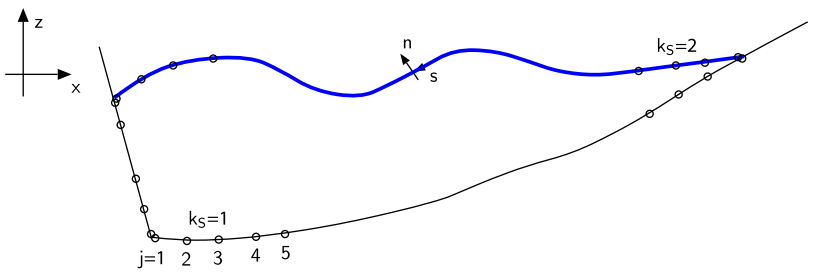

Figure 2. Numerical solution domain.

coordinates (x_j, z_j). Viewing the nodal index j as a monotonically-increasing real variable, s_j may be determined from the calculus identity

$$\frac{\mathrm{d}s}{\mathrm{d}j} = \sqrt{\left(\frac{\mathrm{d}x}{\mathrm{d}j}\right)^2 + \left(\frac{\mathrm{d}z}{\mathrm{d}j}\right)^2} \tag{9}$$

and numerical integration with initial conditions $s = 0$ at $j = 1$ (see Figure 2). Numerically exact precision, consistent with that sought in the evaluation of the Green's integral, is approached by adopting an error-correcting, adaptive step size ordinary differential equation (ODE) solver [9], with the gradients $\mathrm{d}x/\mathrm{d}j$ and $\mathrm{d}z/\mathrm{d}j$ predicted from cubic spline interpolation from the discrete coordinate pairs (j, x_j) and (j, z_j), respectively. Note that cubic spline interpolation is consistent with Equation (8) local interpolation for ϕ or $\partial\phi/\partial n$.

Some care is necessary in the evaluation of β at the boundary nodes. Given the location of P, at (x_P, z_P), the angle β_j at the node j is

$$\beta_j = \arctan \frac{z_j - z_P}{x_j - x_P} \tag{10}$$

The angle β rotates through a full 2π, with the arctan function providing β in the range $-\pi \leqslant \beta < \pi$. For j positive in the counter-clockwise direction (Figure 1), β will pass through a π to $-\pi$ discontinuity over at least one of the boundary segments. For extreme wave profiles and P located near the water surface, multiple crossings through this π to $-\pi$ discontinuity are possible. At some locations, β may reverse and reverse again through this discontinuity.

The G_B part of Equations (5) and (7) requires that β remains continuous. It requires phase unwrapping, to continuous β values beyond the π to $-\pi$ limits of the arctan function. Where the progression β_{j-1} to β_j passes through the π to $-\pi$ discontinuity, 2π is added to β_j from Equation (10). If these adjustments are made at sequential j nodes around the boundary in the positive counter-clockwise direction, multiple crossings are accommodated.

Two algorithms are introduced for numerical completion of the ΔG_B and ΔG_B local integrals. The first, algorithm A, is broadly representative of common finite element practice [3, 4] for the boundary integral method in water waves, except that the element integrations are completed analytically rather than numerically. Detailed evaluation in the context of moderately extreme steady water waves demonstrates the utility of this common approach throughout the interior of the solution domain. But there are residual difficulties very close to the domain

boundaries, just those regions identified in the introduction as physically and numerically sensitive.

The second, algorithm B, builds on this experience to identify the source of numerical imprecision near the boundary and to introduce a methodology that resolves this difficulty.

There is one over-riding constraint on these and any alternative algorithm for the interior problem II. The algorithm must be suitable for implementation in the boundary problem I, where Green's integral (Equation (3)) must be evaluated for point P on the boundary. In the boundary problem context, either ϕ or $\partial\phi/\partial n$ is unknown at the boundary nodes. Only one of these is a known boundary condition, and the choice will change with the boundary segment. This constraint translates into a requirement that a suitable algorithm must not assume that either ϕ or $\partial\phi/\partial n$ are known at the boundary nodes in the numerical evaluation of Equation (7).

4. ALGORITHM A

Algorithm A writes Equation (5), without approximation, as

$$-2\pi\phi_P = G_B + G_C = \int_S \phi(\beta)\,\mathrm{d}\beta - \int_S \ln r \frac{\partial\phi}{\partial n}\,\mathrm{d}s \tag{11}$$

Equation (6) remains formally unchanged, with the nodal integrands, Equation (7), becoming

$$\Delta G_B|_{i_P,j} = \int_{\beta_j}^{\beta_{j+1}} \phi\,\mathrm{d}\beta, \quad \Delta G_C|_{i_P,j} = -\int_{s_j}^{s_{j+1}} \ln(r)\frac{\partial\phi}{\partial n}\,\mathrm{d}s \tag{12}$$

Algorithm A introduces the presumably consistent assumptions that

1. $\phi(\beta)$ between boundary nodes follows Equation (8) in β rather than s;
2. $\ln(r(s))$ in G_C is available at the same boundary nodes as ϕ or $\partial\phi/\partial n$, and;
3. interpolation of $\ln(r(s))$ between boundary nodes again follows Equation (8) in s.

With cubic interpolation for $\phi(\beta)$, the first term in Equation (12) may be evaluated analytically. Conveniently, the result can be written as the linear sum

$$\Delta G_B|_{i_P,j} = b_{i_P,j-1}\phi_{j-1} + b_{i_P,j}\phi_j + b_{i_P,j+1}\phi_{j+1} + b_{i_P,j+2}\phi_{j+2} \tag{13}$$

The coefficients $b_{i_P,j-1}$ through $b_{i_P,j+2}$ are relatively simple algebraic functions of the known location of P and the known $\beta_{i_P,j-1}$ through $\beta_{i_P,j+2}$ at boundary nodes $j-1$ through $j+2$. They do not require that ϕ be known at the boundary nodes. Equation (13) respects the constraint that neither ϕ nor $\partial\phi/\partial n$ be known in advance at the boundary nodes.

With cubic interpolation for $\partial\phi/\partial n|(s)$ and for $\ln r|(s)$, the second term in Equation (12) may also be evaluated analytically. Conveniently, this result can also be written as the linear sum

$$\Delta G_C|_{i_P,j} = c_{i_P,j-1}\frac{\partial\phi}{\partial n}|_{j-1} + c_{i_P,j}\frac{\partial\phi}{\partial n}|_j + c_{i_P,j+1}\frac{\partial\phi}{\partial n}|_{j+1} + c_{i_P,j+2}\frac{\partial\phi}{\partial n}|_{j+2} \tag{14}$$

The coefficients $c_{i_P,j-1}$ through $c_{i_P,j+2}$ are moderately complicated algebraic functions of the known location of P and the known s_{j-1} through s_{j+2} at boundary nodes $j-1$ through

$j+2$. The coefficients were determined by computer algebra. Equation (14) also respects the constraint that neither ϕ nor $\partial\phi/\partial n$ be known in advance at the boundary nodes.

Note that local analytical integration is possible in evaluation of all parts of Equation (7) inter-nodal integration. The same procedure is followed for starting inter-nodal integrals (integration from s_{j_F} to s_{j_F+1}) over a segment, and for concluding inter-nodal integrals (integration from s_{j_L-1} to s_{j_L}) over a segment. Beyond the local cubic interpolation for ϕ, $\partial\phi/\partial n$, β and $\ln r$, there are no further assumptions in the evaluation of the Green's integral, the right-hand side of Equation (11).

In finite element practice, it is common to complete both definite integrals in Equation (12) by Gaussian quadrature [10, Section 25.4.29-30]. m-point Gaussian quadrature is exact for polynomial integrands of order $2m$ or less. The contributions to Equation (12) would require 2-point and 3-point Gaussian quadrature, respectively, to match analytical intergration.

5. EXACT KINEMATICS FOR EVALUATION

Three test problems are formulated, each with exact kinematics available for comparison.

The first is a steady flow problem in a wedge-shaped domain. The solution domain is shown in Figure 3. The domain extends over the first quadrant with radius 1 m. The velocity potential function is assigned as

$$\phi(x) = -0.5 + x \tag{15}$$

so that the Cartesian velocity components are $(\partial\phi/\partial x, \partial\phi/\partial z) = (1, 0)$ m/s.

There are three distinct boundary segments, segment 1 along the x-axis from $(0, 0)$ to $(1, 0)$, segment 2 along the constant radius arc from $(1, 0)$ to $(0, 1)$, and segment 3 along the z-axis from $(0, 1)$ back to $(0, 0)$. There are ten equal steps along each boundary segment, with spacing 0.1 along segments 1 and 3 and $\pi/20$ along segment 2. There are double nodes at

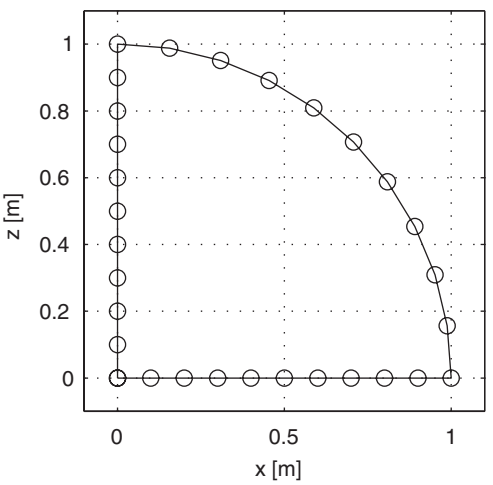

Figure 3. Solution domain for steady flow in open wedge.

Table I. Sample near-limit waves.

Category	h (m)	H (m)	T (s)	$\omega^2 h/g$	H/H_{Limit}
(I) Shallow	2	1.5	10	0.08	0.95
(II) Deep	100	25	10	4.02	0.96

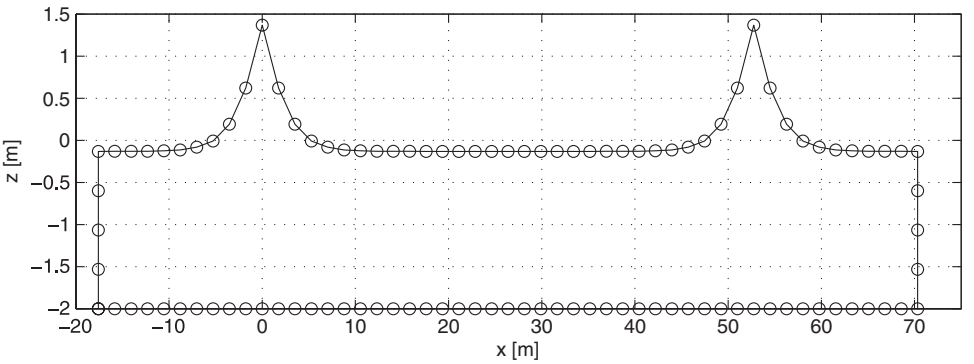

Figure 4. Solution domain for shallow water wave I.

each of the three boundary corners, to accommodate the $\partial\phi/\partial n$ discontinuity at the corners. ϕ remains continuous across the double corner nodes. At each boundary node, both ϕ and $\partial\phi/\partial n$ are specified, consistent with Equation (15).

The second and third problems are much more demanding. They are near-limit waves, the details being listed in Table I. Wave I is in shallow water, Wave II in deep water. Both are within 5% of the limit wave height, H_{Limit}, suggested by the Reference [11] tables. Time t is zero in both cases, h is the water depth, H is the wave height, T is the wave period, $\omega = 2\pi/T$ is the wave frequency and g is the gravitational acceleration. Boundary integral method solutions will be evaluated against steady water wave kinematics from Fourier approximation wave theory [12].

The solution domain for shallow water wave I is shown in Figure 4. The domain extends over $-L/3 < x < 4L/3$, including two crests; L is the wavelength. The space step along the boundary is uniform at $\Delta x = L/30$ in the x direction. It is also uniform in the z direction from the bed to the local water surface at approximately the same magnitude. From a visual perspective, this resolution is sufficient at all locations except perhaps at the wave crests, an issue to which attention will return.

There are four distinct boundary segments, segment 1 along the bed at $z = -h$ from $x = -L/3$ to $x = 4L/3$, segment 2 along the right-hand boundary at $x = 4L/3$ from $z = -h$ to $z = \eta(4L/3, t)$, segment 3 along the water surface from $(x = 4L/3, z = \eta(4L/3, t))$ to $(x = -L/3, z = \eta(-L/3, t))$ and segment 4 at $x = -L/3$ from $z = \eta(-L/3, t)$ back to $z = -h$. At each boundary node, both ϕ and $\partial\phi/\partial n$ are specified from Fourier approximation wave theory. $\partial\phi/\partial n$ is routinely available from the (u, w) velocity component at the boundary nodes and the local boundary orientation. The velocity potential function ϕ is not routinely available from Fourier approximation wave theory, where the stream function Ψ in the steady frame is a dependent variable.

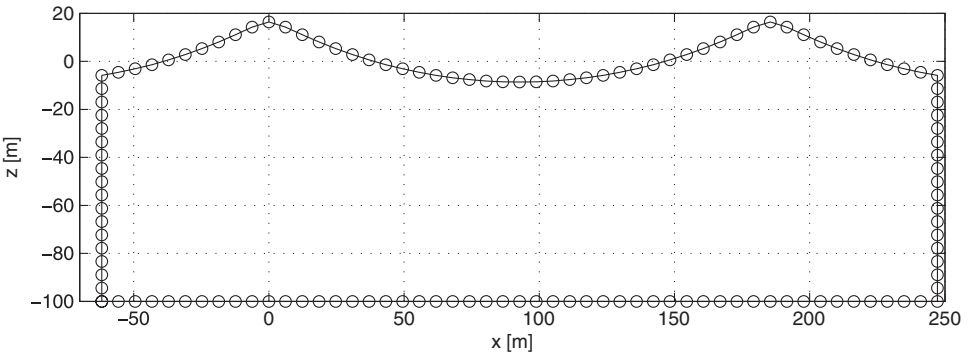

Figure 5. Solution domain for deep water wave II.

In Fourier approximation wave theory [12], the stream function Ψ in the steady frame is

$$\Psi(X,z) = -\bar{U}(h+z) + \frac{g^2}{\omega^3}\sum_{j=1}^{N} B_j \frac{\sinh jk(h+z)}{\cosh jkh}\cos jkX \tag{16}$$

where B_j are the dimensionless Fourier coefficients, of which there are N. $X = x - Ct$ is the horizontal spatial coordinate in the steady frame moving at the phase speed $C, -\bar{U}$ is the current in the steady frame and $k = 2\pi/L$ is the wave number. As both the velocity potential function and the stream function must satisfy the Laplace equation, the velocity potential function in the steady frame is

$$\Phi(X,z) = -\bar{U}X + \frac{g^2}{\omega^3}\sum_{j=1}^{N} B_j \frac{\cosh jk(h+z)}{\cosh jkh}\sin jkX \tag{17}$$

In the unsteady frame, the velocity potential function is

$$\phi(x,z,t) = \Phi(x - Ct, z) + Cx \tag{18}$$

There are double nodes at each of the four boundary corners, to accommodate the $\partial\phi/\partial n$ discontinuity at the corners. ϕ remains continuous across the double corner nodes.

The solution domain for deep water wave II is shown in Figure 5.

6. ALGORITHM A AND EXACT KINEMATICS

For the open wedge domain, numerical solutions were computed for selected horizontal and vertical profiles. Horizontal profiles were computed at $z = 0.5, 0.1$ and 0.01 m. The computational points were uniformly distributed over the available x profile length, with additional near boundary points at $0.1\Delta x$, $0.2\Delta x$ and $0.5\Delta x$ from the boundary at both ends. The vertical profiles were computed at $x = 0.01, 0.1$ and 0.5 m, with computational points distributed over the available z profile length in an analogous manner.

Figure 6 shows the horizontal profiles of $\phi(x;z,t)$ for the exact solution from Equation (15) (solid line) and for the numerical solution from algorithm A (x marker, with dotted line).

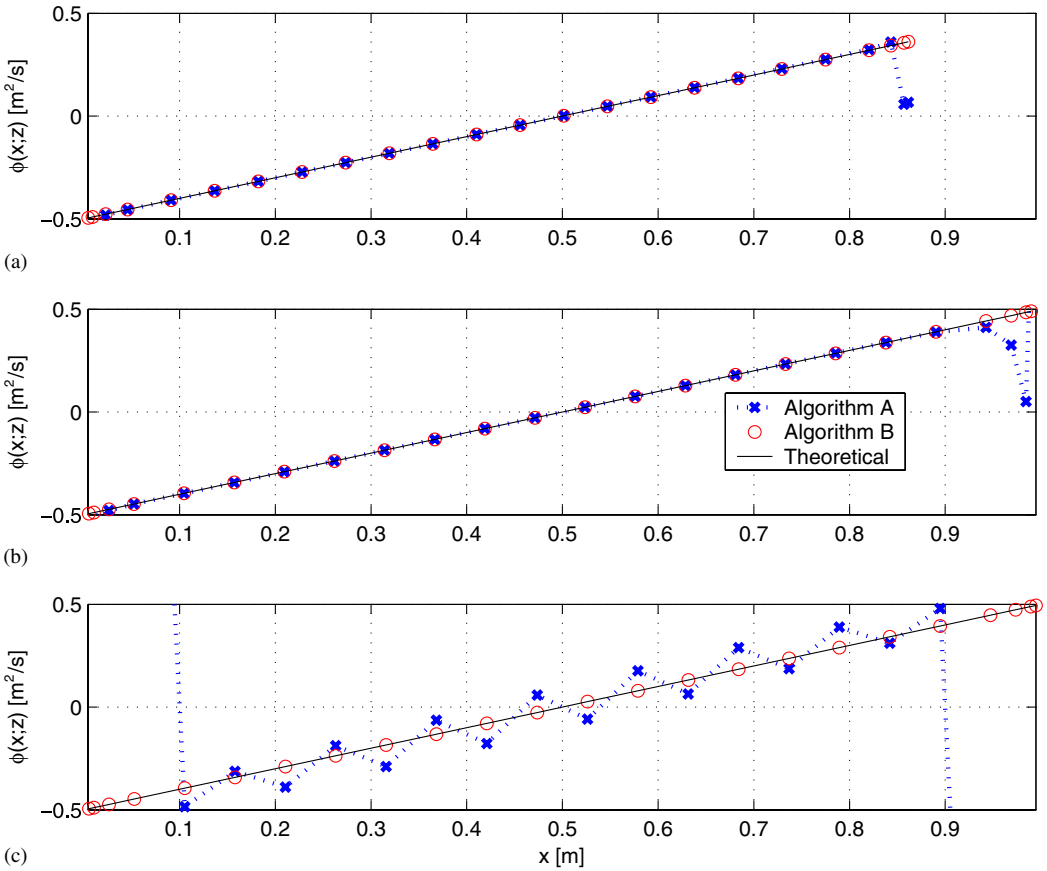

Figure 6. Horizontal profiles for steady flow in open wedge: (a) $z = 0.5$ m; (b) $z = 0.1$ m; and (c) $z = 0.01$ m.

Figures 6(a) and (b) demonstrate a response for Algorithm A that approaches acceptability for field locations somewhat distant from the boundary. This is a consistently reproducible result, that the precision of interior solutions sufficiently distant from the boundary is satisfactory.

But near-boundary solutions are not acceptable. Figure 6(c), 0.01 m inside the lower domain boundary has oscillations of very significant magnitude about the analytical solution, going off-scale at the left and right boundaries. Figures 6(a) and (b) mirror this pattern near the right-hand boundary. This poor precision at near-boundary locations is perhaps widely recognized, but not at all widely acknowledged in the literature. Figure 4 in Reference [13] is a notable exception.

Figure 7 shows the vertical profiles of $\phi(z;x,t)$ for the exact solution from Equation (15) (solid line) and for the numerical solution from algorithm A (x marker, with dotted line). A similar response pattern is repeated. There are upper and lower boundary errors from algorithm A at all locations, and oscillations throughout for the profile at $x = 0.01$ m, very close to the left-hand domain boundary. Distant from the boundary, algorithm A predictions are acceptable.

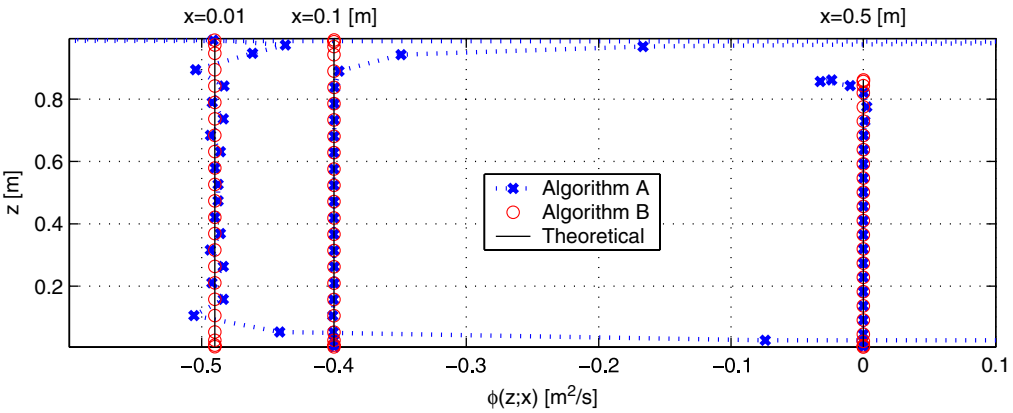

Figure 7. Vertical profiles for steady flow in open wedge.

For the near-limit waves, numerical solutions were computed for selected near-surface longitudinal profiles and for selected vertical profiles. For the near-surface longitudinal profiles, numerical solutions were sought at $z = \eta(x,t) - 0.01H$, $\eta(x,t) - 0.1H$ and $\eta(x,t) - 0.5H$, respectively. The x locations were on a uniform grid of spacing $\Delta x = (5L/3)/20$, supplemented by locations at $-L/3 + 0.01\Delta x$, $-L/3 + 0.1\Delta x$ and $-L/3 + 0.5\Delta x$ at the left-hand end and locations at $4L/3 - 0.5\Delta x$, $4L/3 - 0.1\Delta x$ and $4L/3 - 0.01\Delta x$ at the right-hand end. The finer resolution at the left and right boundaries were intended to capture the near-boundary response at the left and right vertical boundary segments, respectively.

Figure 8 shows the near-surface longitudinal profiles of $\phi(x;z,t)$ for the exact solution from Fourier wave theory (solid line) and for the numerical solution from algorithm A (x marker, with dotted line). Figure 8(c), distant from the boundary, does approach the analytical solution in parts. But an observation from the open wedge solutions, that precision of algorithm A interior solutions sufficiently distant from the boundary is satisfactory, is not appropriate for this near-limit wave example.

Figure 8(a), $0.01H$ below the water surface has oscillations of very significant magnitude (some off-scale) about the analytical solution. These are reduced in Figure 8(b), at $0.1H$ below the water surface, and further reduced in Figure 8(c), at $0.5H$ below the water surface. There are also very significant off-scale errors near both the left- and right-hand boundaries. The crucial role of the water surface in extreme wave kinematics and the lateral boundaries in wave forcing was highlighted in the introduction, together with concerns over numerical precision at just these locations. The Figure 8 result confirms that numerical fidelity at near-boundary locations is a core issue in application of the boundary integral method to extreme wave kinematics.

Figure 8(b) demonstrates one further concern. Note in particular the relatively poor response around $x = 0$ and $x = L$ ($L = 52.7$ m for shallow water wave I). These locations (see Figure 4) correspond to the wave crest where both ϕ and especially $\partial\phi/\partial n$ are rapidly varying with s. Adequate resolution of rapidly changing segments of the boundary conditions is a routine requirement of the problem formulation. Marginal resolution may be recovered

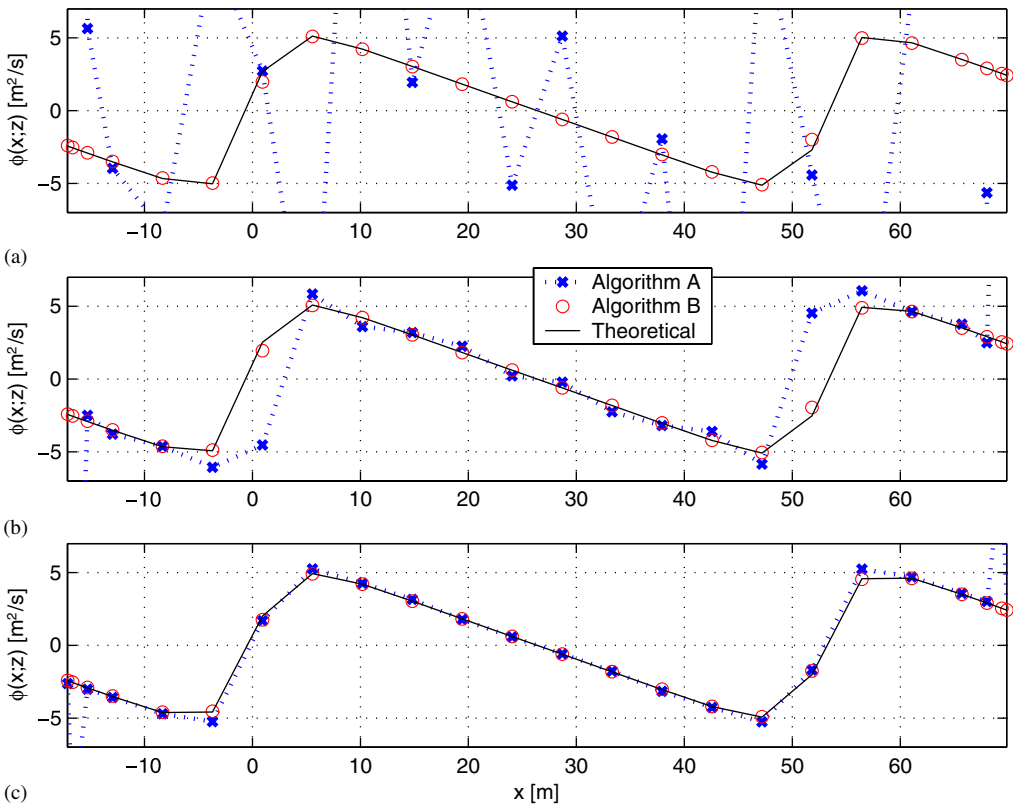

Figure 8. Near-surface longitudinal profiles for shallow water wave I: (a) $z = \eta - 0.01H$; (b) $z = \eta - 0.1H$; and (c) $z = \eta - 0.5H$.

by the implicit boundary interpolation, but this is not guaranteed. This result corresponds with a visual appreciation of the Figure 4 solution domain—boundary resolution seems adequate at all locations with the possible exception of the neighbourhood of the two wave crests. While enhanced spatial resolution around the crests may improve the response around $x = 0$ and $x = L$ in Figure 8(b), it will have little impact on the overall near boundary response.

Figure 9, also for shallow water wave I, shows vertical profiles at $x = 0.1L$ and at $x = 0.2L$, for the exact solution from Fourier wave theory (solid line) and for the numerical solution from algorithm A (x marker, with dotted line). This result is consistent with the near-surface longitudinal profiles above. The response for algorithm A is not acceptable near the water surface and the bed.

Significantly also, numerical precision deteriorates quite markedly in the interior. By a process of elimination and observation of intermediate numerical results, this lack of fidelity in the interior was attributed to rapid changes in η, ϕ and $\partial\phi/\partial n$ along the water surface.

Figure 10, for deep water wave II, shows the near-surface longitudinal profiles of $\phi(x; z, t)$ for the exact solution from Fourier wave theory (solid line) and for the numerical solution from algorithm A (x marker, with dotted line). The algorithm A result generally confirms the

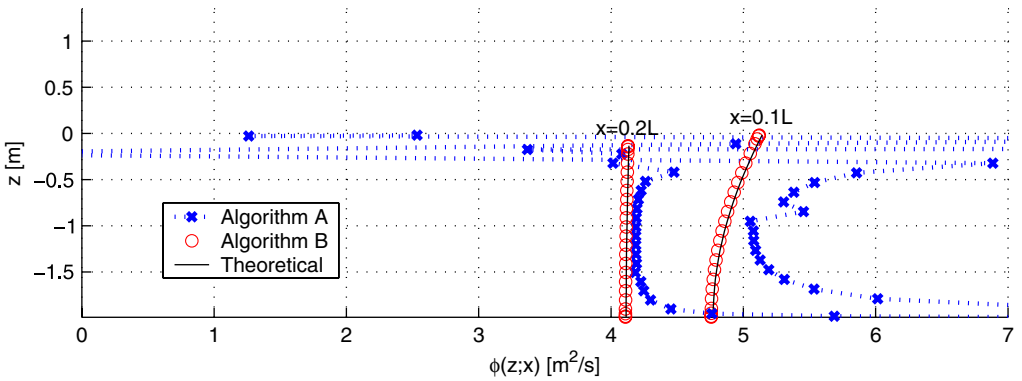

Figure 9. Vertical profiles for shallow water wave I.

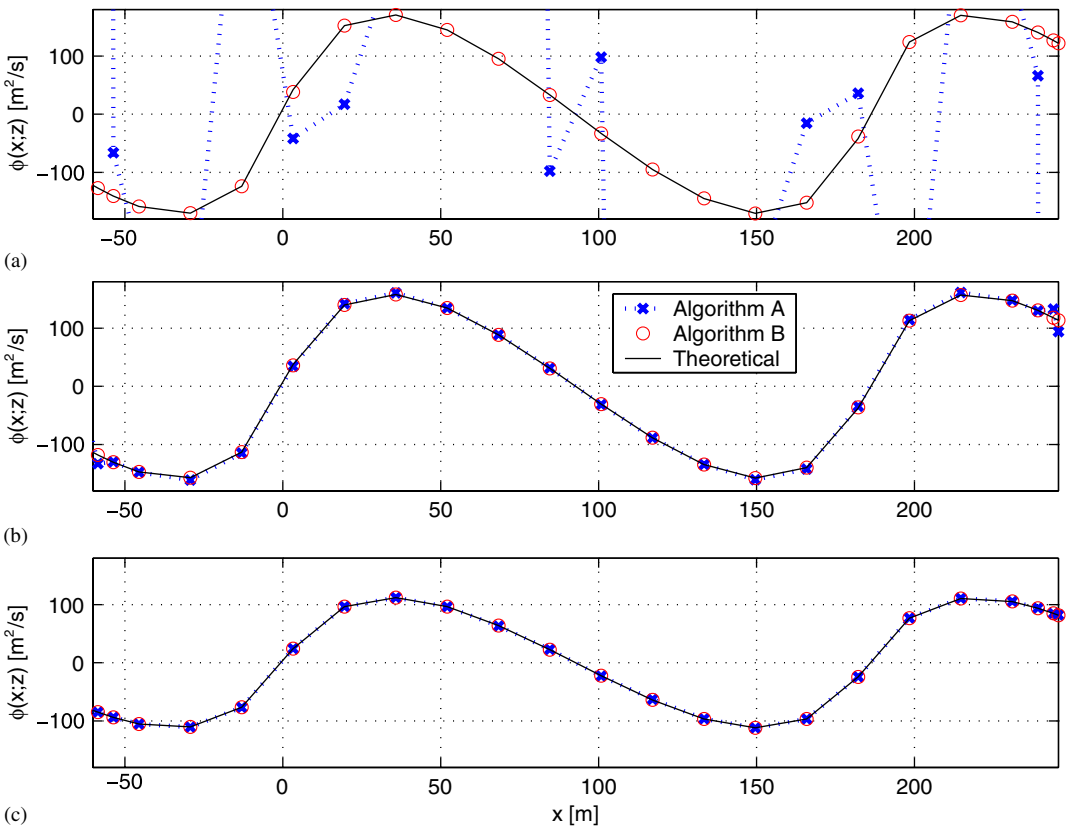

Figure 10. Near-surface longitudinal profiles for deep water wave II: (a) $z = \eta - 0.01H$; (b) $z = \eta - 0.1H$; and (c) $z = \eta - 0.5H$.

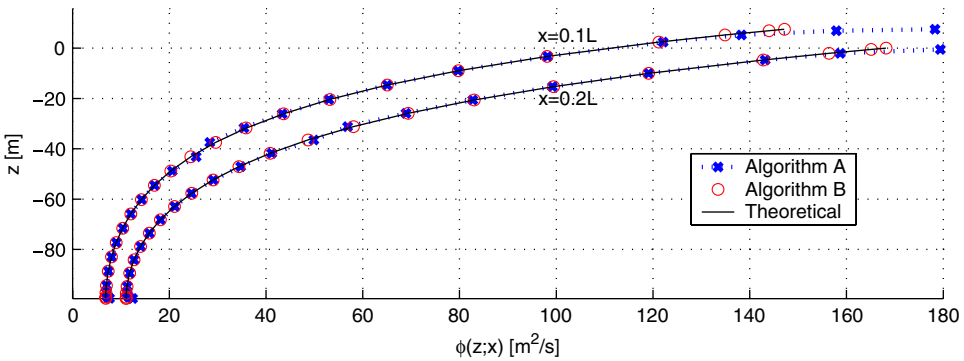

Figure 11. Vertical profiles for deep water wave II.

observations above for the shallow water wave. Crest sharpening for near-limit waves in deep water are rather less extreme than for near-limit waves in shallow water, and the algorithm A numerical solution does much better. It nonetheless remains unacceptable at near-boundary locations.

Figure 11 shows deep water vertical profiles at $x = 0.1L$, and at $x = 0.2L$, for the exact solution from Fourier wave theory (solid line) and for the numerical solution from algorithm A (x marker, with dotted line). Difficulties are again observed near the water surface and at the bed. But the less rapid changes in η, ϕ and $\partial\phi/\partial n$ along the water surface for the deep water wave do not compromise the interior solution to the extent observed in Figure 9.

7. ALGORITHM B

The difficulties encountered with algorithm A, for P near the boundary and for rapid variation of η, ϕ and $\partial\phi/\partial n$ along the water surface, are strictly geometric. While both x_j and z_j vary slowly and smoothly with s or j within a boundary segment, β_j will vary slowly and smoothly with s or j only when P is distant from the boundary and when η, ϕ and $\partial\phi/\partial n$ along the water surface are not rapidly varied.

Spatial resolution around the boundary is typically assigned in an heuristic manner. Regions of known physical and/or numerical challenge, such as steep profile neighbourhoods, a natural shoaling bed, a wave maker board, segment corners, etc. must have adequate nodal density to resolve the more rapid variations. Boundary nodal resolution of sufficient detail to meet these constraints is assumed. This practice results in satisfactory spatial interpolation for x, z, ϕ and $\partial\phi/\partial n$ with s or j. Cubic spline interpolation, consistent with Equation (8), has demonstrated its efficacy in this context.

But much finer resolution of the β variation with s or j is necessary. It is appropriate here to regard j as a real variable, with boundary nodes located at integer values for j. By definition, the boundary coordinate s varies smoothly and monotonically around the boundary. The real variable j will also vary smoothly and monotonically around the boundary, in parallel with s.

Given a continuous $x(j)$ and $z(j)$ prediction, based on cubic spline interpolation from the discrete coordinate pairs (j,x_j) and (j,z_j) at integer j, a very much finer $\beta(j)$ resolution

is available from Equation (10). A j spacing of 0.1 has proved adequate. Given discrete coordinate pairs (j, β_j) at very much finer resolution, cubic spline interpolation was again adopted.

The algorithm constraint, that a suitable algorithm must not assume that either ϕ or $\partial\phi/\partial n$ are known at the boundary nodes, remains.

Algorithm B is based directly on Equation (5), with boundary integration in s for both the G_B and G_C contributions. Substituting Equation (8) for $\phi(s)$, the ΔG_B integral becomes

$$\begin{aligned}\Delta G_B|_{i_P,j} &= \int_{s_j}^{s_{j+1}} (b_0 + b_1 s + b_2 s^2 + b_3 s^3)\frac{\mathrm{d}\beta}{\mathrm{d}s}\,\mathrm{d}s \\ &= b_0\int_{s_j}^{s_{j+1}} \frac{\mathrm{d}\beta}{\mathrm{d}s}\,\mathrm{d}s + b_1\int_{s_j}^{s_{j+1}} s\frac{\mathrm{d}\beta}{\mathrm{d}s}\,\mathrm{d}s + b_2\int_{s_j}^{s_{j+1}} s^2\frac{\mathrm{d}\beta}{\mathrm{d}s}\,\mathrm{d}s + b_3\int_{s_j}^{s_{j+1}} s^3\frac{\mathrm{d}\beta}{\mathrm{d}s}\,\mathrm{d}s \\ &= b_0B_0 + b_1B_1 + b_2B_2 + b_3B_3 \end{aligned} \tag{19}$$

where

$$B_0 = \int_{s_j}^{s_{j+1}} \frac{\mathrm{d}\beta}{\mathrm{d}s}\,\mathrm{d}s = \int_{s_j}^{s_{j+1}} \mathrm{d}\beta = \beta(j+1) - \beta(j) \tag{20a}$$

$$B_1 = \int_{s_j}^{s_{j+1}} s\frac{\mathrm{d}\beta}{\mathrm{d}s}\,\mathrm{d}s = \int_{j}^{j+1} s\frac{\mathrm{d}\beta}{\mathrm{d}j}\,\mathrm{d}j \tag{20b}$$

$$B_2 = \int_{s_j}^{s_{j+1}} s^2\frac{\mathrm{d}\beta}{\mathrm{d}s}\,\mathrm{d}s = \int_{j}^{j+1} s^2\frac{\mathrm{d}\beta}{\mathrm{d}j}\,\mathrm{d}j, \quad B_3 = \int_{s_j}^{s_{j+1}} s^3\frac{\mathrm{d}\beta}{\mathrm{d}s}\,\mathrm{d}s = \int_{j}^{j+1} s^3\frac{\mathrm{d}\beta}{\mathrm{d}j}\,\mathrm{d}j \tag{21}$$

The coefficient B_0 is defined, Equation (20a). B_1–B_3 are conveniently evaluated through numerical integration of the simultaneous ordinary differential equations

$$\frac{\mathrm{d}B_1}{\mathrm{d}j} = s\frac{\mathrm{d}\beta}{\mathrm{d}j}, \quad \frac{\mathrm{d}B_2}{\mathrm{d}j} = s^2\frac{\mathrm{d}\beta}{\mathrm{d}j}, \quad \frac{\mathrm{d}B_3}{\mathrm{d}j} = s^3\frac{\mathrm{d}\beta}{\mathrm{d}j} \tag{22}$$

from j to $j+1$, with initial conditions $B_1 = B_2 = B_3 = 0$ at j. s is available from the simultaneous ordinary differential Equation (9). $x(j)$, $z(j)$ and $\beta(j)$ are available as continuous functions of j from cubic spline interpolation, with β at suitably fine resolution. The gradients $\mathrm{d}x/\mathrm{d}j$, $\mathrm{d}z/\mathrm{d}j$ and $\mathrm{d}\beta/\mathrm{d}j$ are also available from the same cubic spline algorithms. Note in particular that numerical integration of Equations (22) requires only that adequately precise estimates of s and $\mathrm{d}\beta/\mathrm{d}j$ at each real j be available. Importantly, there is no restriction on the manner of their prediction, permitting the mixture of cubic spline interpolation at differing j densities (x and z at integer value of j, β at enhanced resolution) and numerical integration for s.

The definite integrals for B_1 (Equation (20b)), B_2 and B_3 (Equation (21)) might potentially be completed by Gaussian quadrature but how to assign the appropriate m-point order is not clear. m would need to be in double digits to achieve the required enhanced resolution for β. Numerical integration of Equations (22) avoids this issue, through an error-correcting, adaptive step-size ODE solver.

As before (Equation (8)), the coefficients b_0–b_3 are evaluated uniquely from the local ϕ value at consecutive nodes s_{j-1}, s_j, s_{j+1}, s_{j+2}. With known B_0–B_3, Equation (19) becomes

$$\Delta G_B|_{i_P,j} = b_{i_P,j-1}\phi_{j-1} + b_{i_P,j}\phi_j + b_{i_P,j+1}\phi_{j+1} + b_{i_P,j+2}\phi_{j+2} \tag{23}$$

The coefficients $b_{i_P,j-1}$–$b_{i_P,j+2}$ are moderately complicated algebraic functions of the known location of P, the known s_{j-1}–s_{j+2} at boundary nodes $j-1$–$j+2$, and the known B_0–B_3. The coefficients were determined my computer algebra. Equation (23) respects the constraint that neither ϕ nor $\partial\phi/\partial n$ be known in advance at the boundary nodes.

Similarly substituting Equation (8) for $\partial\phi/\partial n$, the ΔG_C integral becomes

$$\begin{aligned}\Delta G_C|_{i_P,j} &= -\int_{s_j}^{s_{j+1}} (c_0 + c_1 s + c_2 s^2 + c_3 s^3)\ln r \,\mathrm{d}s \\ &= -c_0\int_{s_j}^{s_{j+1}} \ln r \,\mathrm{d}s - c_1\int_{s_j}^{s_{j+1}} s\ln r \,\mathrm{d}s - c_2\int_{s_j}^{s_{j+1}} s^2\ln r \,\mathrm{d}s - c_3\int_{s_j}^{s_{j+1}} s^3\ln r \,\mathrm{d}s \\ &= -c_0C_0 - c_1C_1 - c_2C_2 - c_3C_3 \end{aligned} \tag{24}$$

where

$$C_0 = \int_{s_j}^{s_{j+1}} \ln r \,\mathrm{d}s = \int_{s_j}^{s_{j+1}} \ln r \frac{\mathrm{d}s}{\mathrm{d}j}\,\mathrm{d}j, \quad C_1 = \int_{s_j}^{s_{j+1}} s\ln r \,\mathrm{d}s = \int_{j}^{j+1} s\ln r \frac{\mathrm{d}s}{\mathrm{d}j}\,\mathrm{d}j \tag{25}$$

$$C_2 = \int_{s_j}^{s_{j+1}} s^2\ln r \,\mathrm{d}s = \int_{j}^{j+1} s^2\ln r \frac{\mathrm{d}s}{\mathrm{d}j}\,\mathrm{d}j, \quad C_3 = \int_{s_j}^{s_{j+1}} s^3\ln r \,\mathrm{d}s = \int_{j}^{j+1} s^3\ln r \frac{\mathrm{d}s}{\mathrm{d}j}\,\mathrm{d}j \tag{26}$$

The coefficients C_0–C_3 are conveniently evaluated through numerical integration of the simultaneous ordinary differential equations

$$\frac{\mathrm{d}C_0}{\mathrm{d}j} = \ln r\frac{\mathrm{d}s}{\mathrm{d}j}, \quad \frac{\mathrm{d}C_1}{\mathrm{d}j} = s\ln r\frac{\mathrm{d}s}{\mathrm{d}j}, \quad \frac{\mathrm{d}C_2}{\mathrm{d}j} = s^2\ln r\frac{\mathrm{d}s}{\mathrm{d}j}, \quad \frac{\mathrm{d}C_3}{\mathrm{d}j} = s^3\ln r\frac{\mathrm{d}s}{\mathrm{d}j} \tag{27}$$

from j to $j+1$, with initial conditions $C_0 = C_1 = C_2 = C_3 = 0$ at j. s is available from the simultaneous ordinary differential Equation (9). As before, $x(j)$, $z(j)$, $\mathrm{d}x/\mathrm{d}j$, and $\mathrm{d}z/\mathrm{d}j$ are available as continuous functions of j from cubic spline interpolation. $\mathrm{d}s/\mathrm{d}j$ is again available from the simultaneous ordinary differential Equation (9).

As before (Equation (8)), the coefficients c_0–c_3 are evaluated uniquely from the local $\partial\phi/\partial n$ value at consecutive nodes s_{j-1}, s_j, s_{j+1}, s_{j+2}. With known C_0–C_3, Equation (24) becomes

$$\Delta G_C|_P = c_{i_P,j-1}\frac{\partial\phi}{\partial n}|_{j-1} + c_{i_P,j}\frac{\partial\phi}{\partial n}|_j + c_{i_P,j+1}\frac{\partial\phi}{\partial n}|_{j+1} + c_{i_P,j+2}\frac{\partial\phi}{\partial n}|_{j+2} \tag{28}$$

The coefficients $c_{i_P,j-1}$ through $c_{i_P,j+2}$ are moderately complicated algebraic functions of the known location of P, the known s_{j-1} through s_{j+2} at boundary nodes $j-1$ through $j+2$, and the known C_0–C_3. The coefficients were again determined by computer algebra. Equation (14) also respects the constraint that neither ϕ nor $\partial\phi/\partial n$ be known in advance at the boundary nodes.

The simultaneous ODE system, Equations (9), (23) and (28) is numerically integrated by an error-correcting, adaptive step size ODE solver [9], at precision consistent with that sought in the evaluation of the Green's integral.

8. ALGORITHM B AND EXACT KINEMATICS

The algorithm B response patterns have been included (the o markers) in Figures 8–11. These results are very acceptable. There is a suggestion around $x=0$ and $x=L$ in Figure 8 for shallow water wave I that nodal resolution around the crests is a little coarse, and this confirms the expectation from Figure 4. There is no such concern for the deep water wave II where nodal resolution around the crests is sufficient.

9. CONCLUSIONS

The predictive capability of the boundary integral method for 2D water wave kinematics in the interior of a domain has been explored. The test cases are steady flow in an open wedge sector and two near-limit waves, respectively, in shallow and deep water. Numerically exact kinematics is available for each of these test cases.

Algorithm A, generally representative of common finite element practice at a cubic order, provided the initial evaluation. The expectation that near-boundary locations are a weak link in the predictive capability of the boundary integral method was confirmed. Additionally, for near-limit waves, predictions of wave kinematics in the interior of the domain were unsatisfactory, especially in shallow water.

The source of these wave-kinematic difficulties was traced to relatively rapid spatial wave oscillations, precisely the situation expected in the prediction of extreme wave kinematics.

These difficulties are geometric in nature and follow from poor resolution of the variation of the angle β (Figure 1) along the boundary. In the prediction of extreme wave kinematics, these geometric difficulties are compounded by the rapid spatial oscillations of the water surface, where β does not always increase monotonically with j, the nodal index anti-clockwise around the boundary (Figure 2).

Significantly enhanced spatial resolution of β_j is essential. The boundary location (x_j, z_j) is relatively slowly varying, such that resolution and spatial interpolation has not been a problem. An order of magnitude better spatial resolution of β_j has proved adequate, and this is available from cubic-spline interpolation of the (x_j, z_j) boundary locations. Careful attention to phase unwrapping at the $+\pi$ to $-\pi$ discontinuity in the arctan function is crucial, especially where β does not increase monotonically with j.

Utilization of this enhanced spatial resolution for β required reformulation of the ΔG_B and ΔG_C boundary integrations as systems of simultaneous ordinary differential equations, Equations (9), (23) and (28). Numerically exact integration follows from classical error-correcting, adaptive step size ODE code.

These geometric and numerical integration enhancements have been incorporated into Algorithm B. Excellent predictive capability is demonstrated for near-limit wave kinematics.

ACKNOWLEDGEMENTS

This research was initiated with financial support from the UK EPSRC, through contract GR/R64971/01(P). Caroline Hague and Lorenzo Stoakes contributed to initial code development.

REFERENCES

1. Longuet-Higgins MS, Cokelet ED. The deformation of steep surface waves on water. A numerical method of computation. *Proceedings of the Royal Society of London*, *Series A* 1976; **350**:1–26.
2. Yeung RW. Numerical methods in free surface flows. *Annual Review of Fluid Mechanics* 1982; **14**:395–442.
3. Grilli ST, Skourup J, Svendsen IA. An efficient boundary element method for nonlinear water waves. *Engineering Analysis with Boundary Elements* 1989; **6**:97–107.
4. Liu PL-F, Hsu H-W, Lean MH. Applications of boundary integral equation methods for two-dimensional non-linear water wave problems. *International Journal for Numerical Methods in Fluids* 1992; **15**:1119–1141.
5. Clément A. Coupling of two absorbing boundary conditions for 2D time-domain simulations of free surface gravity waves. *Journal of Computational Physics* 1996; **126**:139–151.
6. Kim CH, Clément AH, Tanizawa K. Recent research and development of numerical wave tanks. *International Journal of Offshore and Polar Engineering* 1999; **9**:241–256.
7. Grilli ST, Guyenne P, Dias F. A fully non-linear model for three-dimensional overturning waves over an arbitrary bottom. *International Journal for Numerical Methods in Fluids* 2001; **35**:829–867.
8. Lamb H. *Hydrodynamics* (6th edn). Cambridge University Press: Cambridge, MA, 1932.
9. Press WH, Teukolsky SA, Vetterling WT, Flannery BP. *Numerical Recipes in FORTRAN*: *The Art of Scientific Computing* (2nd edn). Cambridge University Press: Cambridge, MA, 1992.
10. Abramowitz M, Stegun IA. *Handbook of Mathematical Functions*. Dover: New York, 1964.
11. Williams JM. *Tables of Progressive Gravity Waves*. Pitman: Boston, MA, 1985.
12. Sobey RJ. Variations on Fourier wave theory. *International Journal for Numerical Methods in Fluids* 1989; **9**:1453–1467.
13. Skourup J. A boundary integral equation model for the development of non-linear water waves and their interaction with structures. *Series Paper 47*, Institute of Hydrodynamics and Hydraulic Engineering (ISVA), Technical University of Denmark, Lyngby, 1989.

